ACS NANO

www.acsnano.org

Nongenetic *in Vivo* Bimodal Neuromodulation via Photothermal Gold Nanorods and a Multifunctional Fiber Neural Probe

Chanwoong Yoon, Yunheum Lee, Gyeonghye Yim, Seung-Woo Lee, Wonryung Lee, Young-Gyun Park, and Seongjun Park*

Cite This: https://doi.org/10.1021/acsnano.6c02201

Read Online

ACCESS | Metrics & More | Article Recommendations | Supporting Information

ABSTRACT: Neuromodulation is central to both fundamental neuroscience and the development of next-generation brain−computer interfaces (BCIs). However, most cell-type-specific neuromodulation strategies rely on genetic approaches such as optogenetics, which, despite their high spatiotemporal precision, can perturb intrinsic neuronal properties and raise concerns regarding off-target effects and gene-expression efficiency, thereby limiting clinical translation. Moreover, achieving true bimodal neuromodulation remains challenging, as single-gene expression typically enables either inhibition or excitation, restricting applications to one-way perturbations rather than bimodal control of neural activity. Here, we establish a nongenetic bimodal neuromodulation platform by integrating cholesterol-functionalized gold nanorods (GNR-CLS) with a multifunctional fiber-based neural (MFN) probe for localized photothermal stimulation and validate its functionality in the mouse brain. The MFN probe combines microfluidic delivery, near-infrared (NIR) light transmission, and electrophysiological recording within a single flexible fiber, enabling submillimeter colocalization of nanoparticles and optical stimuli with electrophysiological verification of photothermal neuromodulation. Using this platform, we demonstrate *in vivo* bimodal neuromodulation with both inhibitory and excitatory neuronal responses. Specifically, continuous NIR irradiation suppresses spontaneous firing of GNR-CLS-treated CA1 neurons via activation of thermosensitive inhibitory ion channels, whereas high-intensity NIR pulses delivered to the medial entorhinal cortex elicit spiking activity in the downstream dentate gyrus by transient modulation of membrane capacitance. Neuronal responses are governed by optical pulse parameters, with pulse width and frequency dictating a reversible transition of inhibitory and excitatory neuromodulation. Together, these results demonstrate a fully nongenetic approach to bimodal neuromodulation, enabling both excitatory and inhibitory neuronal control through optical parameter tuning alone.

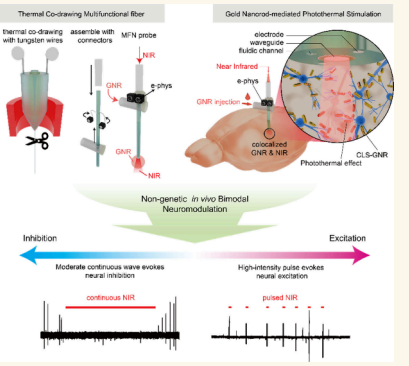

KEYWORDS: *nongenetic neuromodulation, photothermal gold nanorod, multifunctional fiber, in vivo application, thermal drawing process*

Brain engineering technologies have evolved from tools for basic neuroscience research into platforms capable of recording and decoding neural signals to infer cognitive states or motor intentions and translate them into external device control, thereby expanding the scope of human−digital interaction.[1−3] However, progress in brain engineering has been driven predominantly by advances in neural readout, whereas comparatively limited progress has been achieved in neuromodulation for precise control of brain activity or delivery of feedback to neural circuits. Consequently, most existing brain interfaces, although effective as neural decoding systems, remain insufficient for actively manipulating neural circuit states or supporting bidirectional interaction. This imbalance reflects fundamental limitations of current neuromodulation strategies and leaves contemporary brain-machine/computer interface (BMI/BCI) systems largely operating as unidirectional information-processing interfaces.

Electrical stimulation represents the earliest generation of neuromodulation technologies and remains the only modality that has achieved widespread clinical adoption to date.[4−9] While electrical stimulation is effective and comparatively safe, it is inherently constrained by poor spatial and temporal

Received: February 3, 2026
Revised: July 1, 2026
Accepted: July 1, 2026

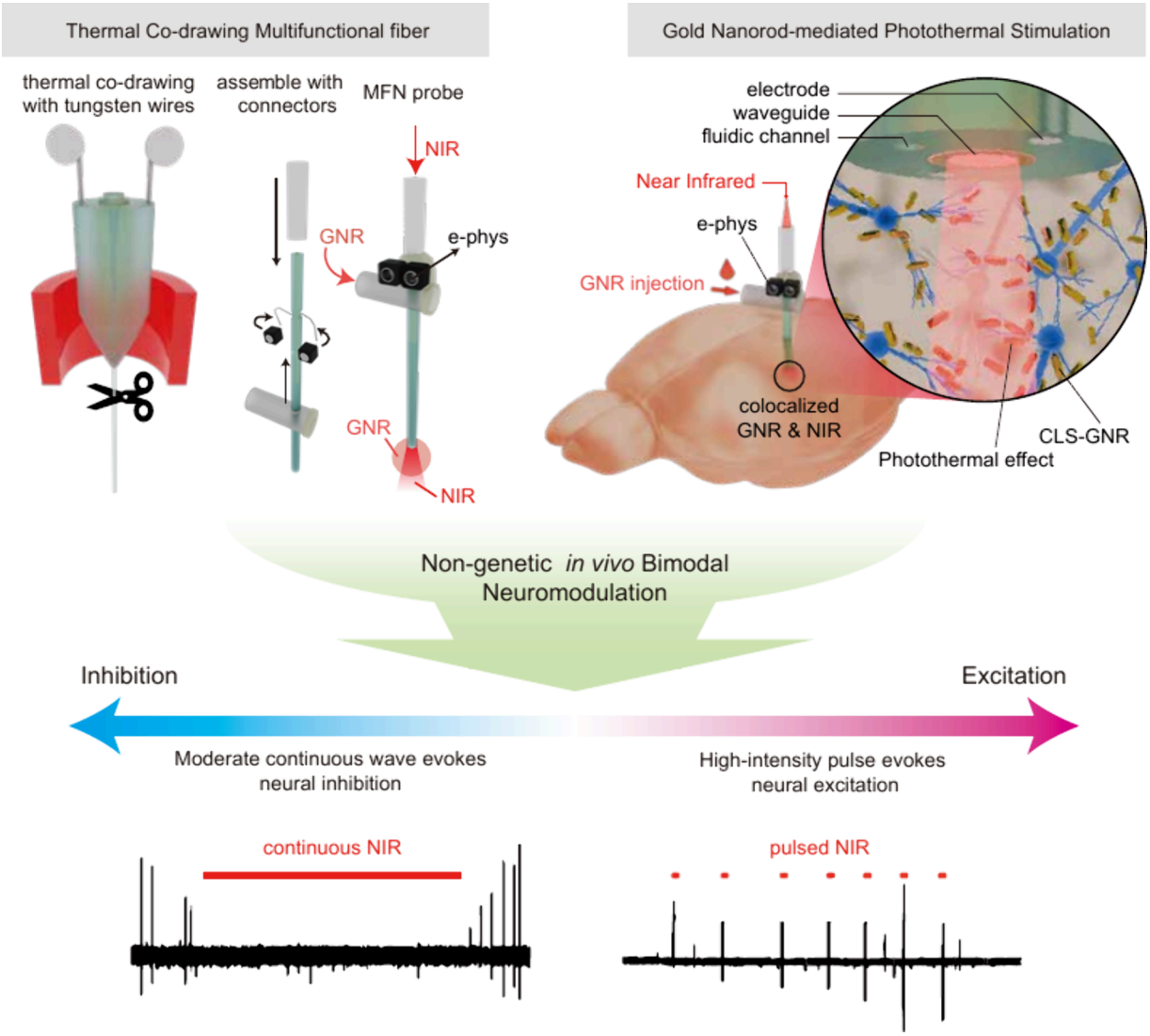

Figure 1. Schematic overview of nongenetic *in vivo* bimodal neuromodulation. A multifunctional fiber-based neural (MFN) probe integrated with cholesterol-functionalized gold nanorods (GNR-CLS) enables nongenetic bimodal neuromodulation *in vivo*. The probe was fabricated by thermal co-drawing of thermoplastic polymers with embedded tungsten microwires, allowing spatially colocalized microfluidic delivery of GNR-CLS, NIR optical stimulation, and electrophysiological recording. Continuous, moderate NIR irradiation suppresses neuronal activity, whereas high-intensity pulsed NIR stimulation induces neuronal excitation.

specificity, resulting in relatively coarse and nonspecific neural modulation.[10,11] In contrast, genetic approaches such as optogenetics have substantially expanded neuromodulation capabilities, enabling control of neuronal activity on millisecond time scales with spatial resolution on the order of tens of micrometers.[12−14] Following viral delivery, artificially expressed ion channels allow host cells to be activated or inhibited by light that does not naturally modulate neuronal activity, thereby enabling cell-type-specific neuromodulation.[15−20]

Despite these advantages, genetic neuromodulation faces several fundamental limitations that hinder its translational potential. First, reliance on viral vectors introduces regulatory, safety, and feasibility challenges for clinical application.[21,22] Second, functional neuromodulation typically requires several weeks to achieve sufficient expression of exogenous channels. Third, implementing both excitation and inhibition often necessitates coexpression of multiple actuators or the use of distinct viral vectors, complicating surgical and transfection procedures.[18−20] These constraints have motivated the search for nongenetic neuromodulation strategies that can be rapidly deployed and support flexible, bimodal control, supporting both excitatory and inhibitory modulation without reliance on genetic modification.

In this perspective, nanoparticle-mediated neuromodulation technologies are emerging as they enable the nongenetic neuromodulation by converting tissue-penetrant physical fields into localized signals that act on wild-type neurons. Piezoelectric barium titanate nanoparticles transduce ultrasound-induced strain into electric fields that activate ion channels and can suppress epileptiform activity.[23,24] Magnetoelectric nanoparticles convert alternating magnetic fields into electric potentials for deep-tissue stimulation, driving neuronal firing and modulating behavior *in vivo*.[25] Magnetic nanoparticles and nanodiscs operate through magnetothermal activation of thermosensitive channels such as TRPV1[26] or magneto-mechanical torque on mechanosensitive channels,[27] while nanozymes catalytically tune redox-sensitive signaling.[28,29]

https://doi.org/10.1021/acsnano.6c02201
ACS Nano XXXX, XXX, XXX−XXX

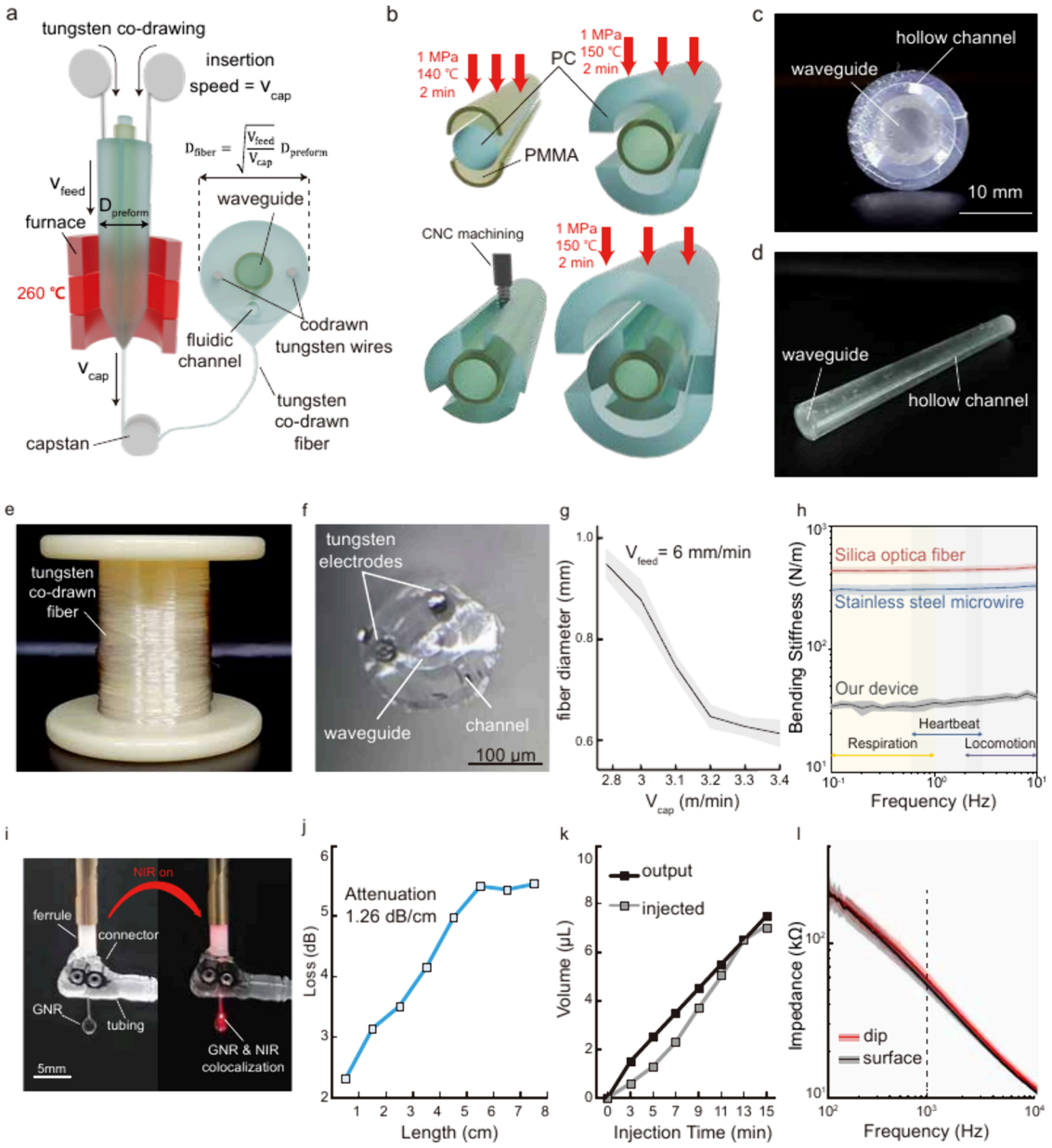

Figure 2. Fabrication and characterization of MFN probe. (a) Schematic illustration of the thermal co-drawing process used to fabricate multifunctional fibers. (b) Schematic of the preform preparation process. (c, d) Cross-sectional (c) and side view (d) images of the polymer preform prior to drawing. (e) Massively drawn, spooled multifunctional fiber. (f) Cross-sectional images of the thermally co-drawn multifunctional fiber. (g) Diameter of the co-drawn fibers as a function of the capstan speed (2.8−3.4 m/min) at a fixed feed speed (6 mm/min); shaded areas indicate standard deviation. (h) Bending stiffness of the multifunctional fiber compared with silica optical fibers and stainless-steel wire in comparable diameter (~300 μm); shaded areas indicate standard deviation. (i) Photograph of the assembled MFN probe, enabling inherent colocalization of GNR delivery and NIR stimulation. (j) Optical transmission loss of MFN probe as a function of probe length yielding an attenuation coefficient was measured as 1.26 dB/cm. (k) Microfluidic performance of MFN probe evaluated by measuring the return rate through microfluidic channel. (l) Impedance spectra of the embedded tungsten electrode in the MFN probes; shaded areas indicate standard deviation. Scale bars: 10 mm (b), 100 μm (f), and 5 mm (i).

Together these approaches offer scalable, minimally invasive alternatives to optogenetic and electrode-based systems. Among these nanoparticles, gold nanoparticle−mediated photothermal neuromodulation provides a distinct physical mechanism for modulating neural activity without genetic manipulation. Because photothermal effects originate directly from the nanoparticles, neuromodulation can be initiated immediately after delivery, bypassing delays associated with genetic expression. Moreover, tuning nanoparticle morphology enables shifting of plasmonic resonance from the visible to the near-infrared (NIR) regime, allowing deep-penetrant and site-specific photothermal stimulation.

Importantly, photothermal heating can induce either inhibition or excitation of neuronal activity depending on stimulation conditions. Moderate and continuous NIR irradiation of gold nanorod−treated hippocampal neurons suppresses neuronal activity through activation of thermosensitive potassium channels such as TREK-1.[30−32] Conversely, strong and brief laser pulses applied to gold nanosphere−treated neurons elicit action potentials by generating rapid

https://doi.org/10.1021/acsnano.6c02201
ACS Nano XXXX, XXX, XXX−XXX

thermal transients that modulate membrane capacitance.[33−35] These complementary mechanisms suggest that selective switching between neuronal inhibition and excitation could, in principle, be achieved within a single system by tuning optical stimulation parameters alone. However, these prior studies[30−32,34,35] have been limited to demonstrating either excitation or inhibition in isolation, and exclusively under *in vitro* conditions, leaving it unestablished whether switchable bimodal neuromodulation can be achieved in intact neural circuits.

A major barrier to *in vivo* validation is the stringent requirement for precise colocalization of nanoparticles, optical stimulation, and electrophysiological recording. Because the effectiveness of thermal energy transfer from GNRs to the plasma membrane diminishes drastically as the distance between the nanorod and the membrane increases,[34] GNRs must be delivered by injecting the GNR colloid directly into the region of interest to enable tight attachment to the plasma membrane. However, unlike viral expression strategies, which progressively expand the effective stimulable volume, nanoparticles remain confined to the injection site, necessitating submillimeter spatial precision. Addressing this challenge requires a multifunctional neural probe that integrates localized delivery of gold nanoparticle colloids, NIR optical stimulation, and electrophysiological electrodes to directly verify photothermal neuromodulation at the same site.[14]

Here, we present an integrated approach that enables nongenetic *in vivo* bimodal neuromodulation, encompassing both excitation and inhibition, in the mouse brain via localized photothermal stimulation (Figure 1). This platform combines a multifunctional fiber-based neural probe with biofunctionalized gold nanorods (GNRs). The probe is fabricated using a thermal co-drawing process that simultaneously scales down a thermoplastic polymer preform while embedding tungsten microwires. This architecture integrates microfluidic channels, an optical waveguide, and tungsten electrodes within a single flexible fiber, thereby providing all key functionalities required for *in vivo* photothermal neuromodulation. The experiments show that cholesterol-functionalized gold nanorods (GNR-CLS) delivered through the microfluidic channel exhibit strong affinity for the plasma membrane, facilitating efficient photothermal coupling to neuronal membranes.[35] Photothermal stimulation through the integrated waveguide induces bimodal neuromodulation in GNR-treated neurons, suppressing spontaneous firing under continuous NIR irradiation and eliciting spiking activity in downstream neural circuits under high-intensity pulsed stimulation. Notably, these effects were achieved within 5 days after implantation - a period allocated solely to allow recovery from mechanical stress due to the probe implantation and GNR injection - in sharp contrast to genetic approaches that typically require weeks of expression prior to functional experimentation. These results establish an immediately deployable, nongenetic platform for bimodal control of neural activity and provide a technological foundation for next-generation, fully bidirectional brain−computer interfaces.

RESULTS AND DISCUSSION

Fabrication of Multifunctional Fiber through Thermal Co-Drawing

To enable precise *in vivo* colocalization of nanoparticle delivery and optical stimulation while minimizing positional drift arising from tissue−probe mechanical mismatch,[36,37] we fabricated a flexible multifunctional fiber-based neural probe that integrates microfluidic channels, an optical waveguide, and conductive electrodes within a single fiber. The multifunctional fiber was fabricated by thermally co-drawing a macroscopic template (preform) together with tungsten microwires (diameter, 25 μm). This approach enables miniaturization of the preform design from the macroscale to the microscale while preserving the cross-sectional architecture and simultaneously embedding metal microwires during thermal drawing (Figure 2a, Figure S1). Prior to thermal drawing, the preform was constructed through sequential stacking and consolidation of thermoplastic polymers (Figure 2b). Polycarbonate (PC) and poly(methyl methacrylate) (PMMA) were selected as matched materials owing to their comparable glass transition temperatures (PC: 137−154 °C; PMMA: 105−120 °C)[38,39] and consequently, similar rheological behavior during thermal drawing.

Importantly, the higher refractive index of PC relative to PMMA (nPC = 1.577−1.587, nPMMA = 1.485−1.492)[38,39] enables formation of a polymer optical waveguide. To construct the waveguide, PMMA half-tubes were stacked around a PC rod and consolidated by hot pressing (1 MPa, 140 °C, 2 min). PC half-tubes were subsequently stacked and consolidated around the waveguide (1 MPa, 150 °C, 2 min), after which three grooves were machined. A sacrificial PC half-tube was subsequently stacked and consolidated (1 MPa, 150 °C, 2 min), enclosing grooves to form hollow channels and complete the preform assembly. The assembled preforms had a diameter of 15.87 mm and a length of 200−230 mm, featuring a central polymer waveguide surrounded by three hollow channels. During the subsequent thermal co-drawing process, these channels were either filled with tungsten microwires to form embedded metal electrodes or left hollow to serve as microfluidic channels. (Figure 2c, d).

The assembled preform was suspended in a fiber-drawing tower and heated to 260 °C, above the glass transition temperature of constituent polymers. Stable thermal co-drawing process by careful tuning of the drawing parameters yielded approximately 100 m of multifunctional fiber with high uniformity (Figure 2e). Cross-sectional analysis of the resulting fibers exhibited an approximately two-order-of-magnitude reduction in overall dimensions, resulting in the waveguide core area of 0.0105 ± 0.0014 mm^2. This confirms well-defined spatial organization of the optical waveguide and microfluidic channels, as well as robust embedded and electrically insulated tungsten microwires within the fiber. The architecture enables precise spatial colocalization of optical irradiation and fluid delivery while ensuring sufficiently low electrode impedance for electrophysiological recording (Figure 2f).

A key feature of the thermal co-drawing process is the ability to systematically control fiber dimensions through adjustment of processing parameters. In particular, increasing the capstan speed resulted in a corresponding reduction in overall fiber diameter. Under a fixed feed rate of 6 mm min^{-1}, increasing the capstan speed from 2.8 to 3.4 m min^{-1} reduced the preform diameter from 15.88 mm to a range of 950.0−614.2 μm (Figure 2g), with further reductions achievable at higher capstan speeds. In this regime, the optical waveguide core diameter ranged from 113 to 128 μm, while the microfluidic channel diameters ranged from 18 to 35 μm. The resulting tungsten co-drawn multifunctional fibers exhibited high mechanical flexibility, with bending stiffness values of 32.96−

https://doi.org/10.1021/acsnano.6c02201
ACS Nano XXXX, XXX, XXX−XXX

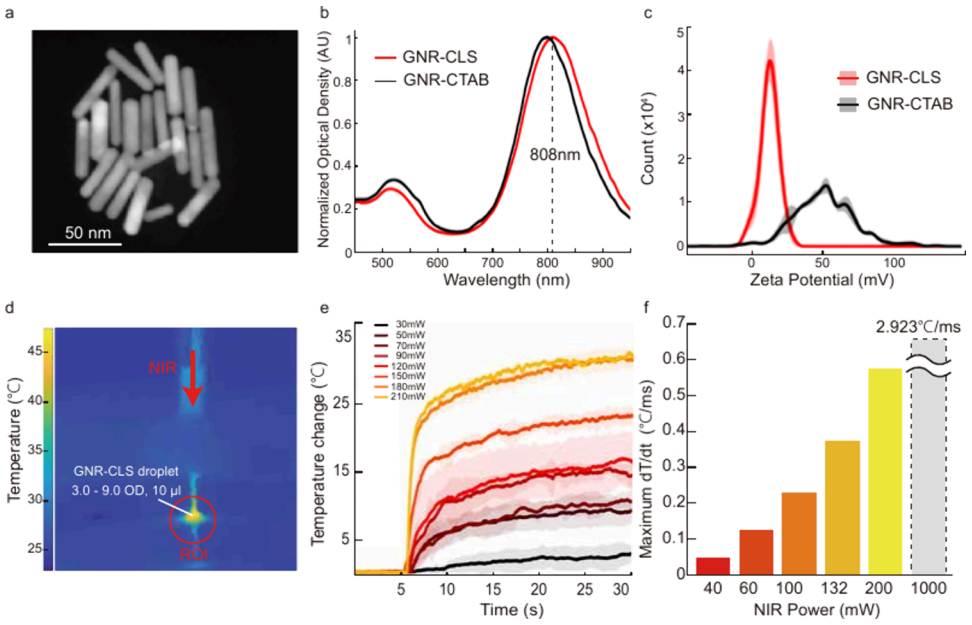

Figure 3. Synthesis, functionalization and characterization of GNR-CLS. (a) Scanning transmission electron microscopy (STEM) image of GNRs. (b) UV−vis absorbance spectra for GNR-CTAB and GNR-CLS, showing preservation of the plasmonic resonance peak after cholesterol functionalization. (c) Zeta potential measurements of GNR-CTAB and GNR-CLS, indicating successful ligand exchange from CTAB to cholesterol-terminated PEG. (d) IR thermal image of GNR-CLS photothermal stimulation delivered through the MFN probes under NIR irradiation. (e) Temperature increases of the GNR droplet with concentration of 3.0 OD during continuous NIR irradiation at different optical power levels, showing power-dependent heating and plateau formation. (f) Maximum temperature change rate of the GNR microdroplet with concentration of 9.0 OD, with the peak heating rate occurring at the onset of NIR irradiation. Scale bars: 50 nm (a).

43.32 N m^{-1} across the frequency range corresponding to respiration, heartbeat, and locomotion (0.01−10 Hz) (Figure 2h). These values are substantially lower than those of silica optical fibers (430.09−461.74 N m^{-1}) or stainless-steel wires (300.39−325.62 N m^{-1}) of comparable dimensions. This remarkably reduced stiffness is expected to mitigate repetitive tissue strain arising from brain−skull micromotion, thereby minimizing foreign body responses, chronic inflammation and glial scarring.[14,40] By more closely matching the mechanical properties of neural tissue, the probes are expected to preserve stable probe−tissue interfaces and positional fidelity within the stimulable region over extended implantation periods.[36,37,41]

Optical, Microfluidic, Electrical Properties of the MFN Probe

From the fabricated multifunctional fibers, segments with diameters ranging from 287 to 338 μm are cut and assembled with silicone tubing, optical ferrules, and socket electrode to form a multifunctional fiber-based neural (MFN) probe with a total weight of 0.6−0.65 g (Figure 2i). The assembled probes were interfaced with external hardware, including a syringe pump, an NIR laser, and data acquisition (DAQ) system, enabling delivery of GNRs, NIR irradiation, and electrophysiological recording, respectively.

In contrast to conventional optogenetic systems that primarily utilize visible wavelengths from blue to deep red, the MFN probe operates in the NIR regime (808 nm) to evoke localized surface plasmon resonance (LSPR) in the delivered gold nanorod. The integrated polymer waveguides of MFN probe exhibited efficient transmission, with measured attenuation of 1.26 dB/cm (Figure 2j), which remained comparable across wavelengths spanning from deep red to near-infrared (620−980 nm) (Figure S2).

Microfluidic performance was evaluated by infusing water through tubing connected to the fiber's microfluidic channel and measuring the output volume. At an infusion rate of 0.5 μL/s, the system achieved a return rate of 94.6% relative to the injected volume (Figure 2k). The maximum fluid volume contained within a single microfluidic channel was 15.3 ± 3.3 μL; however, by connecting the channels to an external pump via tubing, the total deliverable volume is not intrinsically limited.

Electrode impedance measured at 1 kHz ranged from 60.8 to 84.8 kΩ (Figure 2l). Given that reliable electrophysiological recordings with electrodes of 10−20 μm dimensions typically required impedances below ∼ 0.5−1 MΩ,[42−44] these values fall well within the range required for stable neural signal acquisition. Moreover, the impedance remained constant regardless of the probe insertion depth in phosphate-buffered saline (PBS) (Figure S3), confirming effective electrical insulation of the embedded electrodes.

Synthesis and Characterization of Cholesterol-Functionalized Gold Nanorods

To enable photothermal stimulation, gold nanorods (GNRs) were synthesized and subsequently functionalized with cholesterol to improve biocompatibility and cellular adhesion. Following injection into the target region, cholesterol-functionalized gold nanorod (GNR-CLS) act as nanoscale antennas that strongly absorb NIR light and efficiently convert it into heat. Because the surface ligand of nanoparticles critically influences their interactions with biological environment, surface modification is essential for biological applications. GNRs synthesized via conventional seed-mediated methods are typically capped with cetyltrimethylammonium bromide (CTAB),[45] a surfactant known to exhibit cytotoxicity,[46] necessitating ligand exchange prior to *in vivo*

https://doi.org/10.1021/acsnano.6c02201
ACS Nano XXXX, XXX, XXX−XXX

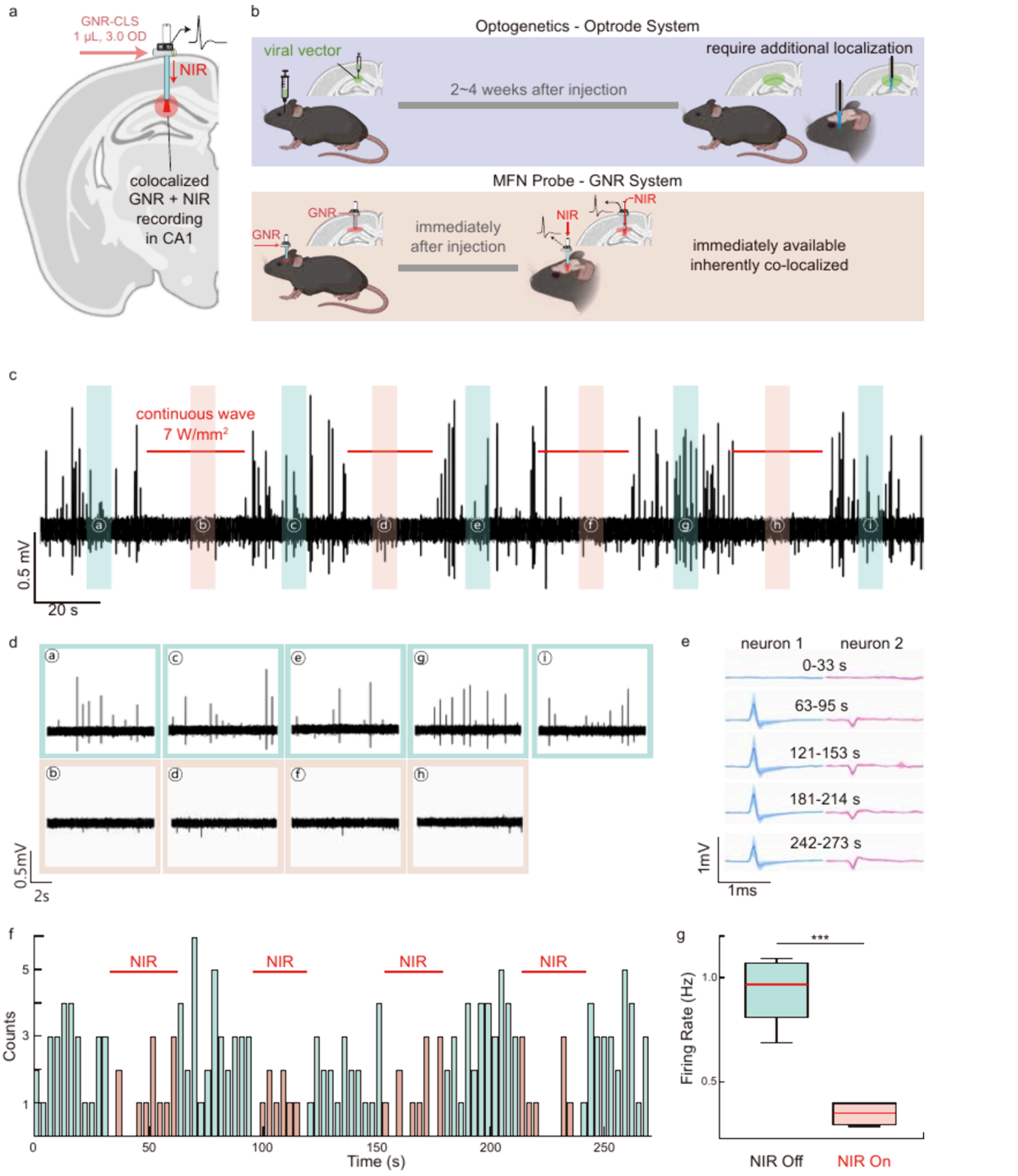

Figure 4. Nongenetic *in vivo* inhibitory neuromodulation. (a) Schematic illustration of the implantation and stimulation paradigm for nongenetic inhibitory neuromodulation in the mouse hippocampal CA1 region. The MFN probe colocalizes NIR irradiation, delivery of GNR-CLS, and electrophysiological recording within CA1. Continuous, moderate NIR irradiation induces localized photothermal effects in GNR-CLS-treated neurons, leading to suppression of spontaneous spiking activity. (b) Conceptual comparison between a conventional optogenetic−optrode system (blue) and the MFN probe−GNR based nongenetic neuromodulation platform (red). (c) Representative single-unit recordings during repeated continuous NIR stimulation (7 W/mm^2); red horizontal bars indicate periods of NIR illumination. (d) Enlarged segment of the single-unit recording, showing reversible suppression of spontaneous firing during NIR irradiation (red box) and recovery in its absence (blue box). (e) Waveforms of spontaneous action potentials recorded in the absence of NIR stimulation after repeated NIR irradiation cycles, showing no detectable change in waveform shape; shaded areas indicate standard deviation. (f) Peri-event time histogram (PETH) of spontaneous activity, showing a marked reduction in bin counts during NIR irradiation (bin size = 3s). (g) Box plot comparing firing rates with and without NIR stimulation, demonstrating significant suppression of spontaneous activity during NIR illumination (t test, ***p < 0.001; p = 0.0003).

use. As a biocompatible alternative, cholesterol-terminated polyethylene glycol (CLS-PEG) was employed. In addition to improving biocompatibility, the positively charged CLS-PEG promotes electrostatic adhesion of GNR-CLS to the plasma

https://doi.org/10.1021/acsnano.6c02201
ACS Nano XXXX, XXX, XXX−XXX

membrane, while the inherent affinity of cholesterol for lipid bilayers further enhances membrane anchoring, thereby improving cellular association and photothermal stimulation efficiency.[35]

Transmission electron microscopy analysis revealed that the GNR-CLS had an average length of 41.43 ± 2.66 nm and a width of 9.86 ± 1.33 nm (Figure 3a). Importantly, cholesterol functionalization did not alter the optical absorbance profile of the nanorods across the visible to NIR spectral range (Figure 3b). In contrast, surface functionalization substantially reduced the surface charge, decreasing the zeta potential from 50.73 ± 21.00 mV to 13.15 ± 6.87 mV (Figure 3c), consistent with successful ligand exchange.[47] Prior to photothermal evaluation, GNR-CLSs were concentrated to 5.76 ± 0.30 × 10^{12} particles mL^{-1} (corresponding to an optical density, OD = 9.0; Figure S4). The photothermal performance of the concentrated GNR-CLSs was evaluated by delivering 10 μL of a GNR- CLS colloid onto parafilm using the multifunctional fiber-based neural probe, while monitoring temperature changes with an infrared camera (Figure 3d). The concentration of GNR colloid was adjusted to replicate the concentration used in the *in vivo* neuromodulation experiment (3.0 OD in Figure 3e; 9.0 OD in Figure 3f). Upon NIR irradiation, the 3.0 OD GNR microdroplet exhibited a rapid temperature increase followed by a stable plateau reaching up to approximately +30 °C (Figure 3e). The pulsed NIR irradiation into 9.0 OD GNR resulted in the maximum temperature change rate of 0.6 °C/ms (Figure 3f). Notably, the highest heating rate occurred immediately upon the onset of NIR illumination.

Although the temperature monitored here may not exactly represent the temperature at the nanorod surface or at the cell membrane, the membrane temperature is expected to be comparable to the medium temperature measured under the conditions of this study for the following reasons. For continuous irradiation, the GNR-CLS act as a dense ensemble rather than as isolated absorbers. In this collective regime, thermal accumulation among neighboring particles averages out the nanoscale single-particle overheating, converging the ensemble, the surrounding medium, and the adjacent membrane to a common steady-state temperature.[48,49] The measured medium temperature is therefore a good representation of the temperature experienced at the membrane under our continuous-stimulation conditions. For pulsed irradiation, the scale of NIR pulse width (μs−ms) greatly exceeds the thermal-diffusion time of single-particle thermal - a few nanoseconds for ∼30 nm rods in an aqueous medium, the nanorods remain in quasi-equilibrium with their immediate surroundings throughout the pulse.[49,50] Therefore, the medium temperature closely tracks the temperature at the nanorod and membrane.

These thermal imaging results therefore demonstrate that GNR-CLS-mediated photothermal stimulation enables precise and tunable control over both transient and steady-state thermal regimes relevant for neuromodulation. Because the photothermal effect of PBS was negligible, the major source of temperature increase is the GNR-CLS (Figure S5).

Nongenetic *in Vivo* Inhibitory Neuromodulation

We next integrated the MFN probe with GNR-CLS to evaluate nongenetic photothermal neuromodulation in the hippocampus of wild-type mice. To first assess the inhibitory modulation, we performed simultaneous single-unit electrophysiological recordings during NIR stimulation in the GNR-CLS-treated CA1 region. The MFN probe was implanted into CA1 (AP = −2.00 mm, ML = ± 1.50 mm, DV = −1.30 mm from bregma), followed by delivery of the GNR-CLS colloid (1 μL, OD = 3.0) through the integrated microfluidic channel (Figure 4a). By spatially colocalizing NIR stimulation, GNR-CLS delivery, and electrophysiological recording within a single platform, the MFN probe enabled concurrent stimulation and recording without the additional alignment procedures typically required for optogenetics optrode system. Moreover, this approach obviates the need for exogenous ion channel expression, allowing neuromodulation to be initiated immediately after a single implantation surgery, in contrast to optogenetic approaches that require weeks of post-transfection expression (Figure 4b). To identify the distribution of GNR, 1 μL of FITC-conjugated GNR was injected, which spread across an elliptical region with a minor axis of 115.04 μm and a major axis of 162.61 μm (Figure S6) in 50 μm-thick slice.

Continuous NIR irradiation at 7 W/mm^2 (70 mW from the waveguide core) elevated the temperature of the 3.0 OD GNR microdroplet by +7 °C above baseline under ambient conditions (Figure 3e, 70 mW). Applying the Pennes bioheat equation for a spherical heat source,[51,52] along with the irradiation parameters extracted by curve fitting temperature change measured by IR camera imaging (Figure S7A), this irradiation is predicted to generate a temperature rise of +6.32 °C at the GNR injection site *in vivo* with full width half-maximum of 0.74 mm (Figure S7B). At this temperature increase, continuous NIR irradiation of the 3.0 OD GNR-treated site produced a pronounced reduction in spontaneous neural activity as recorded by the integrated tungsten electrodes (Figure 4c, Figure S8A). The inhibitory effect was reproducible across repeated stimulation trials, with spontaneous firing consistently suppressed during NIR stimulation (Figure 4d, Figure S8B). Notably, the waveform characteristics of the recorded neural signals remained unchanged across repeated stimulation (Figure 4e, Figure S8C), suggesting that the applied stimulation conditions did not induce detectable tissue damage or adverse effects.

Quantitative analysis further supported these observations. Peri-event timing histogram (PETH; bin size = 3 s) revealed an average spontaneous activity of 2.77 ± 1.18 counts per bin in the absence of NIR stimulation (Figure 4f). During NIR stimulation, the bin count decreased to 1.08 ± 0.97, confirming robust inhibitory modulation. Correspondingly, the mean firing rate decreased significantly from 0.69−1.09 Hz under baseline conditions to 0.29−0.40 Hz during stimulation (t test, ***$p < 0.001$) (Figure 4g).

Because the photothermal effect of PBS was negligible, the injected GNR-CLS is the main source of photothermal stimulation (Figure S5). When the GNR-CLS was replaced with PBS the lack of photothermal effect of PBS resulted in the absence of inhibitory neuromodulation of spontaneous activity (Figure S9). Likewise, no visible inhibition detected in multiunit activity (MUA) in the absence of GNR-CLS (Figure S10A), leaving no difference in the MUA amplitude regardless of the continuous irradiation of 70 mW NIR (Figure S10B). The continuous NIR stimulation evoked significant reduction of MUA amplitude only after the GNR-CLS was injected into the mouse (Figure S10C), with significant difference (Figure S10D). The NIR inhibited neural activity resulted in the reduction of MUA to ∼21% compared to the baseline level only after the GNR-CLS was injected. The inhibition occurred

https://doi.org/10.1021/acsnano.6c02201
ACS Nano XXXX, XXX, XXX−XXX

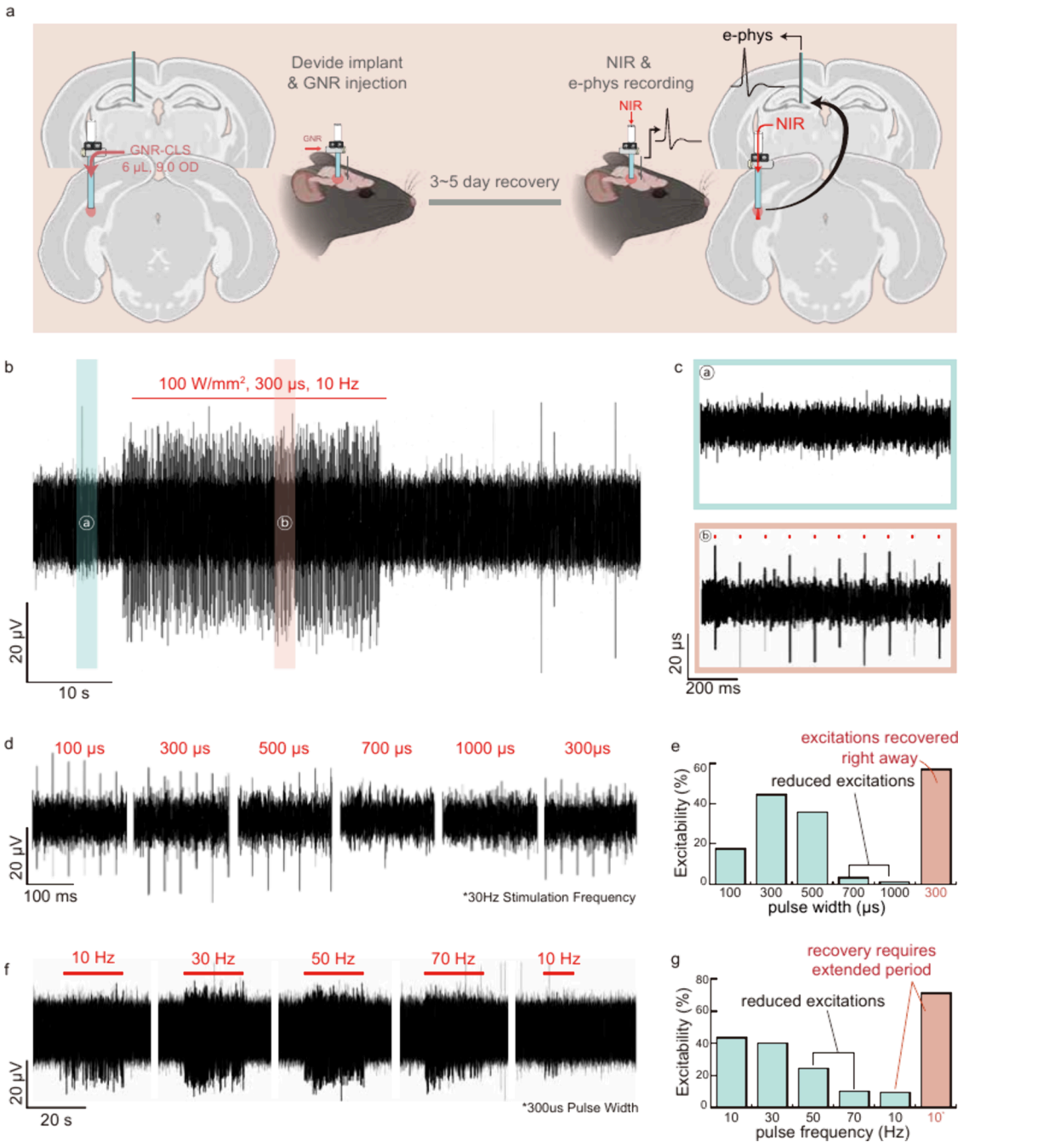

Figure 5. Nongenetic *in vivo* excitatory neuromodulation. (a) Schematic illustration of the implantation and stimulation paradigm for nongenetic excitatory neuromodulation. High-intensity pulsed NIR irradiation is delivered to GNR-CLS-treated neurons in the medial entorhinal cortex (mEC), while electrophysiological recordings are obtained from the dentate gyrus (DG). Spatial separation of stimulation and recording sites minimizes photoinduced artifacts and enables assessment of circuit-level excitation via the monosynaptic mEC−DG projection. The experimental timeline illustrates that GNR-mediated photothermal stimulation can be performed shortly after surgery and nanoparticle delivery. (b, c) Representative single-unit recordings in the DG during high-intensity pulsed NIR stimulation applied to the mEC (power density = 100 W/mm^2, pulse width = 300 μs, stimulation frequency = 10 Hz). Red horizontal bars indicate periods of NIR pulse delivery. Both the full recording (b) and enlarged view (c) show reliable spike evocation in the DG during NIR illumination (SNR = 2.17) (c, inset b) compared to the control without NIR stimulation (c, inset a). Blue and red shaded regions indicate periods without and with NIR stimulation, respectively. (d) Representative recordings of evoked action potentials in the DG under varying NIR pulse widths, showing reduced spike amplitude at excessively long pulse durations. The power density and stimulation frequency were fixed (100 W/mm^2, 30 Hz). (e) Excitability, defined as the probability of spike generation per stimulation pulse, as a function of NIR pulse width; excitability decreases at long pulse widths and recovers upon shortening the pulse width. (f) Representative recordings of evoked action potentials in the DG under varying NIR stimulation frequencies, showing reduced spike amplitude at excessively high frequencies, even immediately after the stimulation frequency is lowered. The power density and pulse width were fixed (100 W/mm^2, 300 μs). (g) Excitability as a function of stimulation frequency, showing frequency-dependent reduction and delayed recovery following high-frequency stimulation.

https://doi.org/10.1021/acsnano.6c02201
ACS Nano XXXX, XXX, XXX−XXX

~ 1.7 s after the NIR onset and returned to the baseline ~4.5 s after the NIR offset (Figure S10E).

Nongenetic *in Vivo* Excitatory Neuromodulation

Next, we evaluated the excitatory capability of the system by applying high-intensity pulsed NIR irradiation to GNR-CLS-treated neurons *in vivo*. The chronic effects of injected GNR-CLS were assessed by immunohistochemistry with NeuN and Iba1 staining after every photothermal stimulation experiment has been completed. The comparison between GNR-CLS injection site and contralateral region revealed no detectable neuronal loss or inflammatory response even after 3 weeks (Figures S11, S12).

To minimize photoinduced artifacts at the stimulation site, we employed a spatially separated stimulation−recording configuration that leveraged the monosynaptic projection from the medial entorhinal cortex (mEC; AP = −4.48 mm, ML = ±3.40 mm, DV = −2.00 mm from brain surface) to the dentate gyrus (DG; AP = −2.00 mm, ML = ±1.20 mm, DV = −2.10 mm from bregma).[53−60] With a separation of approximately 3.5 mm from the stimulation site, the recording electrode reliably captured electrophysiological signals while excluding photoinduced artifacts (Figure S13).

The MFN probe was inserted into mEC, followed by delivery of GNR-CLS (6 μL, OD = 9.0), while an insulated tungsten microwire was positioned in the DG (Figure 5a). This configuration enabled simultaneous photothermal stimulation and electrophysiological recording across two anatomically connected regions, allowing circuit-level excitation induced by pulsed NIR stimulation to be evaluated. As in the inhibitory experiments, the MFN probe colocalized NIR stimulation and GNR-CLS delivery, enabling neuromodulation and recording shortly after a single implantation surgery.

For excitatory neuromodulation, high-intensity NIR pulses (power density = 100 W/mm2; 1000 mW from the waveguide core) were delivered to the GNR-CLS-treated mEC. The temperature change rate at this power density is predicted to be 2.923 °C/ms, an extrapolated value derived from the IR imaging results (Figure 3f). As the pulse duration is sufficiently brief that blood perfusion does not have enough time to meaningfully influence the temperature change, the temperature change rate under *in vivo* conditions is predicted to be comparable. At this temperature change rate, photothermal stimulation reliably evoked spiking activity in the DG (Figure 5b). In control condition without NIR pulses, no evoked spikes were observed (Figure 5c inset a), whereas stimulation elicited clear spikes with a signal-to-noise ratio (SNR) of 2.17 (Figure 5c inset b), confirming effective circuit-level excitation.

To assess the relationship between excitatory efficacy and stimulation parameter, we varied the pulse width (0.1−1 ms) while maintaining the power density (100 W/mm^2) and the stimulation frequency (30 Hz) constant. Photothermal efficacy was quantified by excitability, defined as the probability that a stimulation pulse elicited a spike. Excitability exhibited a strong, but nonlinear dependence on pulse width. Short NIR pulses delivered to the mEC robustly evoked responses in the DG; however, excessively long pulses markedly reduced excitability, which recovered immediately upon shortening the pulse width (Figure 5d). Specifically, excitability was 17.4% at a pulse width of 100 μs and increased to 35.89−44.33% at 300−500 μs, but prolongation reduced excitability to 1.00−3.22%. Restoring the pulse width to 300 μs recovered excitability (Figure 5e). These results suggest that, for short pulses (*e.g.*, 100−300 μs), increasing pulse width increases delivered energy, enhancing membrane heating and transient changes in membrane capacitance, excessively long pulses (*e.g.*, >300 μs), render the heating process more gradual rather than transient, thereby diminishing the ability to induce rapid, transient modulation of membrane capacitance.

We next examined the frequency dependence of excitability by varying the stimulation frequency from 10 to 70 Hz while fixing pulse width at 300 μs. Excitatory efficacy again showed a nonlinear dependence on stimulation frequency. At low to moderate frequencies (10−50 Hz), stimulation reliably evoked spikes time-locked to each NIR pulse. In contrast, at 70 Hz, evoked responses progressively diminished, with a pronounced loss of spiking observed approximately 6 s after stimulation onset (Figure 5f). Notably, unlike the pulse-width dependence, reducing the stimulation frequency did not immediately restore the evoked responses. This effect was more evident in the excitability analysis: excitability remained high at 10−30 Hz (40.17−43.50%), decreased to 24.5% at 50 Hz, and further declined to 10.07% at 70 Hz. Importantly, excitability did not recover immediately upon lowering the stimulation frequency, remaining at 9.5%, and requiring an extended recovery period to return to 71% (Figure 5g). These findings suggest that excessive stimulation frequency induces frequency-dependent neuronal fatigue, potentially arising from cumulative thermal load, activity-dependent ion channel inactivation, or transient metabolic limitations.[61−63] Together, these results demonstrate that excitatory photothermal neuromodulation is robust *in vivo*, but is strongly governed by pulse width and stimulation frequency, highlighting the importance of parameter optimization to maintain stable circuit activation while avoiding fatigue.

To evaluate the thermal effect at the injection site, we performed computational estimation on two distinct time scales: the time-averaged heating accumulated over many pulses, and the transient rise produced by a single pulse. The time-averaged effect is governed by the effective (duty-cycle-weighted) power delivered to the tissue. For a 500-μs pulse width at a 50-Hz repetition rate—the upper bound at which excitatory neuromodulation occurs without reduced excitability—the duty cycle is 2.5%, so 1,000 mW pulsed irradiation corresponds to an effective time-averaged power of 25 mW. Applying the calibration and bioheat model used for the continuous case, but with 3-fold GNR-CLS concentration (×3) and a 10-μL injection volume, this effective power yields an *in vivo* steady-state temperature rise of ~3.0 °C, *i.e.* a peak tissue temperature of ~37.5 °C (Figure S14)—well below the ~40.6 °C threshold for reversible modulation and far below the 43 °C threshold for thermal damage. The corresponding code and results are provided in the Supporting Information. The transient rise during each individual pulse can be estimated as (rate of temperature increase) × (pulse width). At 1,000 mW, the measured heating rate is 2.9 °C ms^{-1}, so a single 500-μs pulse produces a peak rise of ~1.45 °C. This per-pulse increase also lies within the reversible-modulation range and far below the threshold for thermal damage. Taken together, neither the time-averaged heating (~3.0 °C) nor the single-pulse transient (~1.45 °C) approaches the safety limits, confirming that the pulsed-stimulation protocol operates within a thermally safe regime—consistent with the IHC results (Figures S11 and S12).

The major source of photothermal stimulation is the injected GNR-CLS because PBS lacks photothermal effect

https://doi.org/10.1021/acsnano.6c02201
ACS Nano XXXX, XXX, XXX−XXX

(Figure S5). When the GNR-CLS was replaced with PBS, or GNR-CLS was not injected into target region, the lack of photothermal effect resulted in the absence of excitatory neuromodulation of spontaneous activity (Figures S15, S16).

CONCLUSIONS

This work establishes a nongenetic, *in vivo* platform for bimodal neuromodulation by integrating localized photothermal stimulation of cholesterol-functionalized gold nanorods with a multifunctional fiber-based neural probe. By unifying microfluidic nanoparticle delivery, NIR light transmission, and electrophysiological recording within a single flexible device, this approach overcomes a key barrier in nanoparticle-mediated neuromodulation—the precise colocalization of actuators, stimuli, and recording sites in intact brain tissue—and enables neuromodulation immediately after implantation without the delays associated with genetic expression.

Using this platform, continuous NIR irradiation reliably suppressed spontaneous activity in hippocampal CA1 neurons, whereas high-intensity pulsed NIR stimulation elicited circuit-level excitation from the medial entorhinal cortex to the dentate gyrus. The dependence of excitation and inhibition on optical pulse parameters supports a unified photothermal mechanism in which thermal modulation of membrane properties governs neuronal responses, enabling bimodal control through optical tuning alone.

Beyond demonstrating nongenetic bimodal neuromodulation *in vivo*, this work provides a technological foundation for next-generation, bidirectional brain−computer interfaces. The modular design of the MFN probe allows independent optimization of optical, electrical, and fluidic functions, while its low bending stiffness supports stable implantation with minimal tissue disruption. Looking forward, the superior tissue penetration of NIR light compared with visible wavelengths may enable noninvasive photothermal neuromodulation in selected brain regions, thereby reducing reliance on implanted optical components and enhancing translational potential. In parallel, gold nanorods offer versatile surface chemistry that enables functionalization with cell-type-specific ligands or antibodies, providing a route toward selective targeting of defined neuronal populations without the need for viral gene delivery. We also acknowledge that while rigorous biological validation of the proposed mechanisms falls beyond the scope of the present study, it is hoped that the methodology introduced here—together with the clear and reproducible results obtained—will serve as a valuable foundation for future investigations aimed at elucidating the precise biophysical mechanisms underlying GNR-mediated photothermal neuromodulation. Together, this approach lays the groundwork for minimally invasive, nongenetic, and potentially closed-loop neuromodulation systems with translational relevance.

EXPERIMENTAL METHODS

Preform Preparation

The preform, a macroscopic template of fiber, was fabricated via sequential CNC machining, stacking, and thermal consolidation of polycarbonate (PC, McMaster-Carr) and poly(methyl methacrylate) (PMMA, McMaster-Carr). First, polymer tubes (wall thickness: 1.5875 mm) were bisected by CNC milling, during which two longitudinal grooves (3 mm width, 1.5 mm depth) were machined on the exterior. The milling path was offset by 0.2 mm from the tube centerline, yielding asymmetric halves; the larger halves were retained for assembly. This procedure was applied to PC tubes with inner diameters of 9.525 mm (PC half-tube 1) and 12.7 mm (PC half-tube 2), and to PMMA tubes with a 6.35 mm inner diameter. To construct the polymer waveguide, a 6.35 mm-diameter PC rod was aligned with a pair of PMMA half-tubes and consolidated in a hot press (1 MPa, 2 min, 140 °C). PC half-tube 1 sections were then added and consolidated (1 MPa, 2 min, 150 °C), after which three circumferential grooves (1.5 mm width, 1.4 mm depth) were machined around the assembly. Finally, PC half-tube 2 sections were stacked and consolidated (<1 MPa, 1 min, 150 °C) enclosing the grooves to form hollow channels. The resulting preforms matched the outer diameter of PC tube 2 (15.87 mm) and contained three hollow channels surrounding the central polymer waveguide.

Thermal Co-Drawing Process

The multifunctional fiber was fabricated by co-drawing the thermoplastic preform with tungsten microwires using a fiber-drawing tower. Prior to drawing, two 100-m strands of tungsten microwire (25 μm diameter, Goodfellow) were each wound onto pulleys (outer diameter: 30 mm; inner diameter: 8 mm) and threaded through two of the three hollow channels. The microwires were routed to protrude from the opposite end of the preform and fixed in place, before the preform−pulley assembly was mounted onto the tower feeder. A 50 g load was attached to the preform to facilitate initial elongation. The preform was heated to 260 °C to reach its glass-transition state, at which point gravitational extension allowed it to be captured by the capstan. Drawing commenced with a feed speed of 6 mm/min and a capstan speed between 2−10 m/min. As the diameter scaled down during drawing, the shrinking hollow channels closed around the tungsten wires, providing insulation while preserving the overall cross-sectional geometry. The resulting fiber maintained the structural features of the preform and integrated tungsten electrodes, a microfluidic channel, and an optical waveguide.

Assembly into Multifunctional Fiber-Based Neural Probe

The co-drawn multifunctional fibers were assembled with an optical ferrule, electrical socket connectors, and microfluidic tubing to form the multifunctional fiber-based neural (MFN) probe. Sections of the drawn fiber with diameters of 287−338 μm were cut into 5 cm lengths. A small window was then opened at the midpoint of each piece on the side containing the tungsten microwires, after which one wire end was gently extracted while the opposite end remained embedded. The wire-extracted end was designated as the "head" of the probe for optical ferrule attachment, whereas the retained end was designated as the "foot," corresponding to the implanted segment. Two additional windows were carved along the microfluidic channel to expose its interior: one immediately distal from the microwire window toward the foot and a second located 5 mm further toward the foot. After these preparations, the exposed functional components were interfaced with connectors. Tungsten wires were soldered to a two-channel electrical socket connector (Shenzhen Jinling Electronics). A 3 cm silicone tube (wall thickness: 3 mm) with one end sealed by UV-curable resin was positioned such that the foot-side microfluidic window lay inside the tubing while the head-side window remained outside. The fiber head was inserted through an optical ferrule (340-μm bore, Thorlabs) filled with epoxy until slightly protruding from its end. All components—including socket connectors, tubing, and ferrule—were secured to the fiber using UV-curable resin. During this step, the external (head-side) window of microfluidic channel was sealed to ensure that injected fluids exit exclusively though the foot-side window within the tubing. Finally, the protruding fiber tip at the ferrule was trimmed and sequentially polished using 30-μm, 6-μm, and 3-μm grit polishing sheets (Thorlabs), performing 100−150 strokes per grit.

Characterization of Multifunctional Fiber-Based Neural Probe

The assembled MFN probes underwent electrical, microfluidic and optical characterization. The electrical impedance was measured using a benchtop LCR meter (GWINSTEK, LCR-8210). A stainless-steel reference electrode and the MFN probe were immersed in PBS

https://doi.org/10.1021/acsnano.6c02201
ACS Nano XXXX, XXX, XXX−XXX

(ForBioKorea Co.), and impedance was recorded at 1 kHz with a 10-mV excitation. To prevent salt crystallization and subsequent blockage of microfluidic channels, the MFN probe tip was rinsed with DI water immediately after each measurement. Microfluidic characterization was performed by connecting a gastight syringe (Hamilton, 705LT) mounted on a microinjection pump (KD Scientific, KD legato 130 nanosystem) to the MFN probe tubing via PFA tubing (ID = 2 mm, OD = 3 mm) secured with a 1.56 mm connector. Both MFN probe tubing and PFA tubing were prefilled with DI water. The return ratio was determined by injecting fluid at 500 μL/min and measuring the mass of the output fluid every 2 min. The optical loss was measured by optical power meter (Thorlabs, PM100A). The optical ferrule of MFN probe was connected to 808 nm laser (Civil Laser, 808 nm 4000 mW High Power Fiber Coupled Laser IR Laser System) using FC/PC optical patch cord (Thorlabs, core diameter = 200 μm).

Gold Nanorod Synthesis and Functionalization

Gold nanorods (GNRs) were synthesized by conventional seed-mediated growth method[45] which consists of two parts: preparation of seed and growing seed into gold nanorods (GNRs). All solutions were prepared in type-III deionized water (3DI). For seed preparation, 5 mL of 0.2 M cetyltrimethylammonium bromide (CTAB, Sigma-Aldrich) was mixed with 5 mL of 0.5 mM hydrogen tetrachloroaurate-(III) ($HAuCl_4{\cdot}4H_2O$, Sigma-Aldrich) and sonicated (29 °C, 3 min). Subsequently, 600 μL of freshly prepared, ice-cold 10 mM $NaBH_4$ (4 °C, Sigma-Aldrich) was instantaneously added and the mixture was sonicated for an additional 3 min, yielding a seed solution that turns from yellow to brown with slight foaming. The seed solution was kept for 2 h at room temperature before nanorod growth. For nanorod growth, 5 mL of 1 mM $HAuCl_4{\cdot}4H_2O$, 5 mL of 0.2 M CTAB, 270 μL of 4 mM $AgNO_3$ (Sigma-Aldrich), 70 μL of 78.8 mM ascorbic acid, and 12 μL of the seed solution were added sequentially, gently mixing between additions. The growth solution was incubated at 27 °C for 1 h to promote nanorod formation. Excess CTAB was removed by three centrifugation cycles (12,000 RCF, 15 min), each followed by redispersion in 3DI. Cholesterol functionalization was performed via ligand exchange using thiol-PEG_3k-cholesterol (HS-PEG_{3k}-CLS, NanoCS). The GNR colloid was first concentrated to 4.0 OD, after which 1 mL of the colloid was mixed with 200 μL of a 30 mg/mL HS-PEG_3k-CLS solution and incubated overnight with continuous shaking (130 rpm). Excess ligands were removed by at least three centrifugation cycles (12,000 RCF, 15 min) followed by redispersion in 3DI. The resulting cholesterol-functionalized GNRs (GNR-CLS) were concentrated to 9.0 OD and stored at 4 °C.

Measuring Absorbance Profile of GNR Colloids

UV−vis spectroscopy was performed using a microplate reader (SpectraMax, M2e). A 96-well plate (Sigma-Aldrich) was loaded with 200 μL of 3DI water and 200 μL of GNR colloid in separate wells. The optical density of the GNRs was determined by measuring the absorbance of the colloid relative to the 3DI reference.

Measurement of Zeta Potential

Zeta potential was measured by dynamic light scattering (DLS). The GNR colloid was redispersed in 3DI to a concentration of 0.5−1.0 OD, and 800 μL was transferred into a folded capillary cell (Malvern DTC 1070). Measurements were performed using a ZETASIZER Ultra instrument (Malvern, ZETASIZER Ultra).

Temperature Measurement of GNR

The temperature change and its rate were measured by recording thermal images using an IR camera (A350, FLIR). Because camera focusing significantly affects the accuracy of temperature measurement, a preliminary focusing procedure was performed to align the center of the region where the photothermal effect occurs with the camera's focal plane. Specifically, a reference point was marked at the location where the microdroplet would be deposited, and the IR camera focus was adjusted until the projected dot size was minimized. The MFN probe was then positioned so that its tip nearly contacted the parafilm, placing the waveguide tip at the exact location of the reference mark and thereby ensuring coincidence with the focal plane of the IR camera. The parafilm was then displaced so that the reference mark was removed from the stimulation site to exclude any thermal artifact arising from NIR absorption by the marking material. Then 10 μL of GNR-CLS (concentration 3.0−9.0) was injected via probe and irradiated with NIR to evoke photothermal stimulation. After IR imaging, the maximum temperature value within the region of interest (ROI) was extracted, as the most rapid thermal change occurs at the center of the NIR stimulation site.

Stereotaxic Surgery for Devices Implantation

All animal procedures performed were approved by the guidelines of the Institutional Animal Care and Use Committee of the Seoul National University (SNU-241111-9-1) and Korea Advanced Institute of Science and Technology (KA2020-100). Before surgery, all implants—including reference and ground screws (diameter = 1 mm, stainless steel), the MFN probe, and insulated wires—were sterilized by being sprayed with 70% ethanol (EtOH, Clover Chemical) and subsequently placed in a UV sterilizer for at least 2 h. Anesthesia was induced using inhaled isoflurane (ISO, HANA PHARM) mixed with air. Mice were placed in an induction chamber and exposed to 4% ISO for 10 min, after which they were transferred to a two-arm stereotaxic frame (RWD Life Science) set with the heating pad (Reptions) and maintained at 1.2−2% ISO. Fur over the surgical area was removed using electric clippers followed by depilatory cream. Petroleum jelly (Vaseline) was applied to the eyes to prevent drying. The exposed skin was sterilized with iodine using a cotton swab. From this step onward, every tool contacting the skin or skull was sterilized using a bead sterilizer (ALLSHENG, 250 °C, 10 s) before usage. The scalp and connective tissue were then removed to expose the skull, which was disinfected with 3% hydrogen peroxide (DAEJUNG). Craniotomies were drilled for device implantation and screw placement. For device craniotomies, the dura was carefully removed using precise forceps (Fine Science Tools, Dumont #5sf) after which Vaseline wells were constructed around the opening and filled with PBS (ForBioKorea, diluted into 1x PBS) to prevent tissue drying. Ground and reference screws were secured at separated craniotomies (ground: contralateral frontal lobe, AP +1.5 to +2.0 mm; reference: contralateral occipital lobe, AP −3.0 to −4.0 mm), avoiding major neurovascular structures.[64] Before the implantation of MFN probe, its tubing was filled with GNR colloid (3.0−9.0 OD) and connected to a gastight syringe (Hamilton, 705LT) mounted on a microinjection pump (KD Scientific, KD legato 130 nanosystem). Implantation coordinates for the devices were as follows: medial entorhinal cortex (mEC): AP −4.48 mm, ML ±3.4 mm from bregma, DV −2.00 mm from the brain surface; dentate gyrus (DG): AP −2.00 mm, ML ±1.2 mm, DV −2.20 mm; CA1: AP −2.00 mm, ML ±1.5 mm, DV −1.30 mm from bregma. For mEC targeting, DV was referenced to the brain surface rather than bregma to improve placement consistency and mitigate variability arising from cortical curvature. Prior to the implantation, GNR-CLS colloid is loaded into the silicone tubing of the MFN probe. One end of a separate length of PTFE tubing, prefilled with mineral oil, is then connected to a Hamilton syringe filled with deionized water, and the other end is connected to the silicone tubing of the MFN probe via a tubing adapter. Because GNR-CLS within the silicone tubing leaks through the MFN probe tip during this connection step, implantation is performed only after waiting approximately 3−5 min until no further leakage is observed. Then, devices were implanted at the rate <10 μm/s, and GNRs were injected at 80−100 nL min^{-1} (total volume 1−6 μL). After injection, the skull was sealed with SuperBond (sun medical) and overlaid with dental cement (Vertex) to secure the implants and screws. Mice were allowed to recover for at least 3 days before chronic recordings.

Electrophysiological Recording with NIR Stimulation

All electrophysiological recordings were performed under anesthesia within a Faraday cage (KWONSYS). Anesthesia was induced with 4% isoflurane (ISO) in air and reduced to 2% after securing the mouse in a stereotaxic frame. For the electrophysiological recording, the ISO concentration was subsequently lowered to 0.5−1.0% and stabilized for 10 min. For single-unit recordings, signals were band-pass filtered

https://doi.org/10.1021/acsnano.6c02201
ACS Nano XXXX, XXX, XXX−XXX

at 500−5000 Hz using the ZC-16 headstage (LabRat) and a custom EMI-shielded wire assembly connecting the socket connectors of MFN probe to the ZCA-DIP headstage adapter (ZCA-DIP). An 808 nm laser (Civil Laser; output wavelength: 808 ± 5 nm; output power: ∼4W; power stability: <3% per 2 h; temperature stabilizing: TEC; warm up time <5 min; FC/PC interface; 200um core diameter; modulation: 0−30 kHz TTL) was coupled to the MFN probe optical ferrule via an FC/PC connector with a 200-μm core. For the inhibition experiment, the laser was switched to CW mode and the power was adjusted so that NIR of 70 mW power could be output from the waveguide core. For the excitation experiment where pulsed irradiation is required, laser was switched to TTL mode and connected to a function generator that outputs the pulse waveform. Pulsed stimulation was delivered through TTL signals generated by a function generator (rise/falling time = 20 ns, Vpp = 5 0.1 V).

Immunohistochemistry on Paraffin-Embedded Tissue

After completion of all recording sessions, mice were perfused with 4% paraformaldehyde (PFA; Sigma-Aldrich) for fixation. Brains were postfixed in 4% PFA for 20 h, rinsed with deionized water, and processed for paraffin embedding. Paraffin-embedded brain tissues were sectioned at a thickness of 4 μm and subjected to immunohistochemical staining following standard deparaffinization, antigen retrieval, and antibody incubation procedures. Sections were deparaffinized by immersion in xylene (3 min × 3; Sigma-Aldrich) and rehydrated through a graded ethanol series (100% ethanol, 3 min × 2; 95% ethanol, 3 min; 70% ethanol, 3 min), followed by rinsing under cold running tap water. Antigen retrieval was performed by submerging the sections in Tris−EDTA buffer (pH 9.0; Abcam) containing 0.05% Tween-20 (Sigma-Aldrich) and heating in a microwave oven at 1500 W for 2.5 min, with buffer replenishment as needed to compensate for evaporation. Slides were allowed to cool to room temperature before further processing. After antigen retrieval, sections were washed twice for 5 min in wash buffer (PBS containing 0.025% Triton X-100; Sigma-Aldrich). Tissue boundaries were delineated using a hydrophobic barrier pen (PAP pen, Sigma-Aldrich), and nonspecific binding was blocked by incubation in 10% normal donkey serum (NDS; Abcam) in PBS for 2 h at room temperature. Without rinsing, excess blocking solution was gently removed, and sections were incubated overnight at 4 °C with primary antibodies (Abcam) diluted 1:500 in PBS containing 1% bovine serum albumin (Sigma-Aldrich). The following day, sections were washed twice for 5 min in wash buffer and incubated with appropriate Alexa Fluor−conjugated secondary antibodies (Abcam) for 2 h at room temperature in the dark. Slides were then rinsed three times for 5 min in PBS, counterstained with DAPI-containing mounting medium, and coverslipped for confocal imaging.

Control Electrophysiological Recording in PBS Confirming the Absence of Photoinduced Artifacts

A major challenge in electrophysiological recording during high-intensity pulsed NIR stimulation is the generation of photoinduced artifacts (PIAs). To mitigate PIAs, the stimulation and recording sites were spatially separated. Nevertheless, given the extremely high-power density used (100 W/mm^2), residual optical energy could still reach the recording site at a separation of approximately 3.5 mm and potentially be misclassified as neural spikes. To determine whether the recorded spikes originated from PIAs, we performed control recordings in phosphate-buffered saline (PBS) instead of brain tissue (Figure S13A−C). Using the same configuration as in the *in vivo* electrophysiological experiments, the MFN probe was connected to the data acquisition system (DAQ) and NIR laser operating at a power density of 100 W/mm^2, with pulse width was fixed at 500 μs. The insulated tungsten wire was connected to the DAQ as the recording electrode (Figure S13A). The MFN probe and recording electrode were positioned relative to an arbitrarily defined reference point on the PBS surface to replicate the spatial arrangement of the mEC and DG *in vivo* (Figure S13B), and both were fully submerged in PBS. Mediolateral (ML) and anteroposterior (AP) coordinates were defined as relative to an arbitrarily selected reference point, with DV = 0 corresponding to the PBS surface (Figure S13C). If the recorded signals were attributable to PIAs, similar spike-like events would be expected in PBS, as optical scattering and absorption of PBS is substantially lower than biological tissue. At the pseudo-mEC site, where NIR pulses were directly delivered, the recording electrodes exhibited large transient disturbances (Figure S13D, Figure S13E), confirming effective irradiation of the system. In contrast, at the pseudo-DG site, no detectable spikes appeared across all stimulation frequencies (Figure S13F). These results indicate that the spikes recorded in the mouse DG reflect genuine neural activity rather than photoinduced artifacts.

Derivation of Temperature Change and Its Rate under *in Vivo* Conditions from Ambient Measurements

The expected temperature change under *in vivo* conditions was predicted by applying the temperature changes and their rates measured under ambient conditions to the Pennes bioheat equation for a spherical heat source[51,52]).

■ ASSOCIATED CONTENT

Data Availability Statement

All data needed to evaluate the conclusions in the paper are present in the paper and/or the Supporting Information.

Supporting Information

The Supporting Information is available free of charge at https://pubs.acs.org/doi/10.1021/acsnano.6c02201.

Fiber co-drawing tower; optical loss characterization of MFN probes; electrode impedance under different immersion conditions; nanoparticle tracking analysis of gold nanorods; photothermal effect of PBS; distribution of GNR-FITC in CA1; prediction of the *in vivo* steady-state temperature change; inhibitory effect recorded from different channel than in main text; control experiment for inhibition using PBS instead of GNR-CLS; inhibitory neuromodulation before and after GNR-CLS injection (1 μL, 3.0 OD); neuronal integrity in the medial entorhinal cortex after experiments; microglial activation assessment in the medial entorhinal cortex; control electrophysiological recording in PBS confirming the absence of photoinduced artifacts; prediction of the *in vivo* steady-state temperature change due to pulsed irradiation; the result of excitation using PBS instead of GNR; comparison of NIR stimulation with and without GNR injection (PDF)

■ AUTHOR INFORMATION

Corresponding Author

Seongjun Park − *School of Transdisciplinary Innovations, Interdisciplinary Program in Neuroscience, College of Natural Science, Interdisciplinary Program in Bioengineering, College of Engineering, and Interdisciplinary Program in Genetic Engineering, College of Natural Science, Seoul National University, Seoul 08826, Republic of Korea; Department of Biomedical Science, College of Medicine and Medical Research Center, Seoul National University, Seoul 03080, Republic of Korea; Department of Transdisciplinary Medicine, Seoul National University Hospital, Seoul 03080, Republic of Korea;* orcid.org/0000-0002-1981-9628; Email: seongjunpark@snu.ac.kr

https://doi.org/10.1021/acsnano.6c02201
ACS Nano XXXX, XXX, XXX−XXX

Authors

Chanwoong Yoon − *Program of Brain and Cognitive Engineering, Korea Advanced Institute of Science and Technology (KAIST), Daejeon 34141, Republic of Korea*

Yunheum Lee − *Department of Bio and Brain Engineering, Korea Advanced Institute of Science and Technology (KAIST), Daejeon 34141, Republic of Korea*

Gyeonghye Yim − *Department of Bio and Brain Engineering, Korea Advanced Institute of Science and Technology (KAIST), Daejeon 34141, Republic of Korea*

Seung-Woo Lee − *Leesol Co., Ltd., Seoul 06126, Republic of Korea*

Wonryung Lee − *School of Transdisciplinary Innovations, Seoul National University, Seoul 08826, Republic of Korea; Department of Biomedical Science, College of Medicine, Seoul National University, Seoul 03080, Republic of Korea*

Young-Gyun Park − *Department of Bio and Brain Engineering, Korea Advanced Institute of Science and Technology (KAIST), Daejeon 34141, Republic of Korea*

Complete contact information is available at: https://pubs.acs.org/10.1021/acsnano.6c02201

Author Contributions

C.Y. contributed conceptualization, experiments (fiber fabrication, mechanical, electrical characterizations of fibers, preparation of neural probe, gold nanorod synthesis and functionalization, characterization of gold nanorods, implantation surgery, electrophysiological recording with stimulation, immunohistochemistry of NeuN and Iba1, computational simulation), analyses, writing initial draft. Y.L contributed experiments (measurement of bending stiffness), writing initial draft. G.Y. contributed writing initial draft. S.-W.L., W.L., Y.-G.P. contributed supervision. S.P. contributed conceptualization, supervision, writing initial draft.

Notes

The authors declare no competing financial interest.

■ ACKNOWLEDGMENTS

This research was supported by the Korea Brain Research Institute (25-BR-03-02), National Research Foundation of Korea (NRF) funded by Ministry of Science and ICT (RS-2026-25538024, RS-2023-00302489, RS-2026-25474579, 2022M3H4A1A04098817), Boston-Korea Project (RS-2024-00467213) funded by the Korea government (the Ministry of Science and ICT, the Ministry of Health & Welfare), Alchemist Project (RS-2025-02634714) through the Korea Planning & Evaluation Institute of Industrial Technology (KEIT) funded by the Ministry of Trade, Industry and Resources, Startup Growth Technology Development Program (TIPS) funded by the Ministry of SMEs and Startups, Korea, through the Korea Technology and Information Promotion Agency for SMEs (RS-2023-00271419), and Creative-Pioneering Researchers Program through Seoul National University.

■ REFERENCES

(1) Campbell, P. K.; Jones, K. E.; Huber, R. J.; Horch, K. W.; Normann, R. A. A Silicon-Based, Three-Dimensional Neural Interface: Manufacturing Processes for an Intracortical Electrode Array. *IEEE Trans. Biomed. Eng.* **1991**, *38*, 758−768.

(2) Drake, K. L.; Wise, K. D.; Farraye, J.; Anderson, D. J.; BeMent, S. L. Performance of Planar Multisite Microprobes in Recording Extracellular Single-Unit Intracortical Activity. *IEEE Trans. Biomed. Eng.* **1988**, *35*, 719−732.

(3) Musk, E.; et al. An Integrated Brain-Machine Interface Platform with Thousands of Channels. *J. Med. Internet Res.* **2019**, *21*, No. e16194.

(4) Stagg, C. J.; Antal, A.; Nitsche, M. A. Physiology of Transcranial Direct Current Stimulation. *J. ECT* **2018**, *34*, 144−152.

(5) Stagg, C. J.; Nitsche, M. A. Physiological Basis of Transcranial Direct Current Stimulation. *Neuroscientist* **2011**, *17*, 37−53.

(6) Giordano, J.; Bikson, M.; Kappenman, E. S.; Clark, V. P.; Coslett, H. B.; Hamblin, M. R.; Hamilton, R.; Jankord, R.; Kozumbo, W. J.; McKinley, R. A.; Nitsche, M. A.; Reilly, J. P.; Richardson, J.; Wurzman, R.; Calabrese, E. Mechanisms and Effects of Transcranial Direct Current Stimulation. *Dose-Response* **2017**, *15*, 1559325816685467.

(7) Perlmutter, J. S.; Mink, J. W. Deep Brain Stimulation. *Annu. Rev. Neurosci.* **2006**, *29*, 229−257.

(8) Dostrovsky, J. O.; Lozano, A. M. Mechanisms of Deep Brain Stimulation. *Mov. Disord.* **2002**, *17*, S63−S68.

(9) Krauss, J. K.; Lipsman, N.; Aziz, T.; Boutet, A.; Brown, P.; Chang, J. W.; Davidson, B.; Grill, W. M.; Hariz, M. I.; Horn, A.; Schulder, M.; Mammis, A.; Tass, P. A.; Volkmann, J.; Lozano, A. M. Technology of Deep Brain Stimulation: Current Status and Future Directions. *Nat. Rev. Neurol.* **2021**, *17*, 75−87.

(10) Maks, C. B.; Butson, C. R.; Walter, B. L.; Vitek, J. L.; McIntyre, C. C. Deep Brain Stimulation Activation Volumes and Their Association with Neurophysiological Mapping and Therapeutic Outcomes. *J. Neurol., Neurosurg. Psychiatry.* **2009**, *80*, 659−666.

(11) Baizabal-Carvallo, J. F.; Jankovic, J. Movement Disorders Induced by Deep Brain Stimulation. *Parkinsonism Relat. Disord.* **2016**, *25*, 1−9.

(12) Wells, J.; Kao, C.; Konrad, P.; Milner, T.; Kim, J.; Mahadevan-Jansen, A.; Jansen, E. D. Biophysical Mechanisms of Transient Optical Stimulation of Peripheral Nerve. *Biophys. J.* **2007**, *93*, 2567−2580.

(13) Richter, C.-P.; Matic, A. I.; Wells, J. D.; Jansen, E. D.; Walsh, J. T. Neural Stimulation with Optical Radiation. *Laser Photonics Rev.* **2011**, *5*, 68−80.

(14) Park, S.; Guo, Y.; Jia, X.; Choe, H. K.; Grena, B.; Kang, J.; Park, J.; Lu, C.; Canales, A.; Chen, R.; et al. One-Step Optogenetics with Multifunctional Flexible Polymer Fibers. *Nat. Neurosci.* **2017**, *20*, 612−619.

(15) Josselyn, S. A.; Tonegawa, S. Memory Engrams: Recalling the Past and Imagining the Future. *Science* **2020**, *367*, No. eaaw4325.

(16) Nabavi, S.; Fox, R.; Proulx, C. D.; Lin, J. Y.; Tsien, R. Y.; Malinow, R. Engineering a Memory with LTD and LTP. *Nature* **2014**, *511*, 348−352.

(17) Ramirez, S.; Liu, X.; Lin, P.-A.; Suh, J.; Pignatelli, M.; Redondo, R. L.; Ryan, T. J.; Tonegawa, S. Creating a False Memory in the Hippocampus. *Science* **2013**, *341*, 387−391.

(18) Park, S.; Kramer, E. E.; Mercaldo, V.; Rashid, A. J.; Insel, N.; Frankland, P. W.; Josselyn, S. A. Neuronal Allocation to a Hippocampal Engram. *Neuropsychopharmacology* **2016**, *41*, 2987−2993.

(19) Lau, J. M. H.; Rashid, A. J.; Jacob, A. D.; Frankland, P. W.; Schacter, D. L.; Josselyn, S. A. The Role of Neuronal Excitability, Allocation to an Engram and Memory Linking in the Behavioral Generation of a False Memory in Mice. *Neurobiol. Learn. Mem.* **2020**, *174*, No. 107284.

(20) Park, A.; Jacob, A. D.; Walters, B. J.; Park, S.; Rashid, A. J.; Jung, J. H.; Lau, J.; Woolley, G. A.; Frankland, P. W.; Josselyn, S. A. A Time-Dependent Role for the Transcription Factor CREB in Neuronal Allocation to an Engram Underlying a Fear Memory Revealed Using a Novel in Vivo Optogenetic Tool to Modulate CREB Function. *Neuropsychopharmacology* **2020**, *45*, 916−924.

(21) Cox, D. B. T.; Platt, R. J.; Zhang, F. Therapeutic Genome Editing: Prospects and Challenges. *Nat. Med.* **2015**, *21*, 121−131.

(22) Rosenblum, D.; Gutkin, A.; Dammes, N.; Peer, D. Progress and Challenges towards CRISPR/Cas Clinical Translation. *Adv. Drug Delivery Rev.* **2020**, *154*−*155*, 176−186.

(23) Marino, A.; Arai, S.; Hou, Y.; Sinibaldi, E.; Pellegrino, M.; Chang, Y. T.; Mazzolai, B.; Mattoli, V.; Suzuki, M.; Ciofani, G. Piezoelectric Nanoparticle-Assisted Wireless Neuronal Stimulation. *ACS Nano* **2015**, *9*, 7678−7689.
(24) Zheng, Y.; Ju, Y.; Liu, Y.; Yang, F. Piezoelectric Nanoparticle-Based Ultrasound Wireless Piezoelectric Neuromodulation Inhibits Epileptiform Activity of Primary Neurons. *ACS Appl. Bio Mater.* **2024**, *7*, 8543−8551.
(25) Zhang, E.; Abdel-Mottaleb, M.; Liang, P.; Navarrete, B.; Yildirim, Y. A.; Campos, M. A.; Smith, I. T.; Wang, P.; Yildirim, B.; Yang, L.; Chen, S.; Smith, I.; Lur, G.; Nguyen, B. T.; Jin, X.; Noga, B.; Ganzer, P.; Khizroev, S. Magnetic-Field-Synchronized Wireless Modulation of Neural Activity by Magnetoelectric Nanoparticles. *Brain Stimul.* **2022**, *15*, 1451−1462.
(26) Chen, R.; Romero, G.; Christiansen, M. G.; Mohr, A.; Anikeeva, P. Wireless Magnetothermal Deep Brain Stimulation. *Science* **2015**, *347*, 1477−1480.
(27) Gregurec, D.; Senko, A. W.; Chuvilin, A.; Reddy, P. D.; Sankararaman, A.; Rosenfeld, D.; Chiang, P. H.; Garcia, F.; Tafel, I.; Varnavides, G.; Ciocan, E.; Anikeeva, P. Magnetic Vortex Nanodiscs Enable Remote Magnetomechanical Neural Stimulation. *ACS Nano* **2020**, *14*, 8036−8045.
(28) Wu, J.; Wang, X.; Wang, Q.; Lou, Z.; Li, S.; Zhu, Y.; Qin, L.; Wei, H. Nanomaterials with enzyme-like characteristics (nanozymes): next-generation artificial enzymes (II). *Chem. Soc. Rev.* **2019**, *48*, 1004−1076.
(29) Wei, H.; Wang, E. Nanomaterials with enzyme-like characteristics (nanozymes): next-generation artificial enzymes. *Chem. Soc. Rev.* **2013**, *42*, 6060−6093.
(30) Yoo, S.; Park, J.-H.; Nam, Y. Single-Cell Photothermal Neuromodulation for Functional Mapping of Neural Networks. *ACS Nano* **2019**, *13*, 544−551.
(31) Yoo, S.; Kim, R.; Park, J.-H.; Nam, Y. Electro-Optical Neural Platform Integrated with Nanoplasmonic Inhibition Interface. *ACS Nano* **2016**, *10*, 4274−4281.
(32) Yoo, S.; Hong, S.; Choi, Y.; Park, J.-H.; Nam, Y. Photothermal Inhibition of Neural Activity with Near-Infrared-Sensitive Nanotransducers. *ACS Nano* **2014**, *8*, 8040−8049.
(33) Shapiro, M. G.; Homma, K.; Villarreal, S.; Richter, C.-P.; Bezanilla, F. Infrared Light Excites Cells by Changing Their Electrical Capacitance. *Nat. Commun.* **2012**, *3*, 1−11.
(34) Carvalho-de-Souza, J. L.; Treger, J. S.; Dang, B.; Kent, S. B. H.; Pepperberg, D. R.; Bezanilla, F. Photosensitivity of Neurons Enabled by Cell-Targeted Gold Nanoparticles. *Neuron* **2015**, *86*, 207−217.
(35) Carvalho-de-Souza, J. L.; Nag, O. K.; Oh, E.; Huston, A. L.; Vurgaftman, I.; Pepperberg, D. R.; Bezanilla, F.; Delehanty, J. B. Cholesterol Functionalization of Gold Nanoparticles Enhances Photoactivation of Neural Activity. *ACS Chem. Neurosci.* **2019**, *10*, 1478−1487.
(36) Goldstein, S. R.; Salcman, M. Mechanical Factors in the Design of Chronic Recording Intracortical Microelectrodes. *IEEE Trans. Biomed. Eng.* **1973**, *BME-20*, 260−269.
(37) Gilletti, A.; Muthuswamy, J. Brain Micromotion around Implants in the Rodent Somatosensory Cortex. *J. Neural Eng.* **2006**, *3*, 189.
(38) Wypych, G. PC Polycarbonate. In *Handbook of Polymers*; Elsevier: Oxford, 2012; pp 308−314, DOI: 10.1016/B978-1-895198-47-8.50097-7.
(39) Wypych, G. PMMA Polymethylmethacrylate. In *Handbook of Polymers*; Elsevier: Oxford, 2012; pp 450−454, DOI: 10.1016/B978-1-895198-47-8.50136-3.
(40) Hong, G.; Viveros, R. D.; Zwang, T. J.; Yang, X.; Lieber, C. M. Tissue-like Neural Probes for Understanding and Modulating the Brain. *Biochemistry* **2018**, *57*, 3995.
(41) Hassler, C.; Boretius, T.; Stieglitz, T. Polymers for Neural Implants. *J. Polym. Sci., Part B:Polym. Phys.* **2011**, *49*, 18−33.
(42) Ferguson, J. E.; Boldt, C.; Redish, A. D. Creating Low-Impedance Tetrodes by Electroplating with Additives. *Sensors and Actuators, A: Physical* **2009**, *156*, 388−393.
(43) Chung, T.; Wang, J. Q.; Wang, J.; Cao, B.; Li, Y.; Pang, S. W. Electrode Modifications to Lower Electrode Impedance and Improve Neural Signal Recording Sensitivity. *J. Neural Eng.* **2015**, *12*, No. 056018.
(44) Neto, J. P.; Baião, P.; Lopes, G.; Frazão, J.; Nogueira, J.; Fortunato, E.; Barquinha, P.; Kampff, A. R. Does Impedance Matter When Recording Spikes with Polytrodes? *Front. Neurosci.* **2018**, *12*, 408156.
(45) Nikoobakht, B.; El-Sayed, M. A. Preparation and Growth Mechanism of Gold Nanorods (NRs) Using Seed-Mediated Growth Method. *Chem. Mater.* **2003**, *15*, 1957−1962.
(46) Alkilany, A. M.; Nagaria, P. K.; Hexel, C. R.; Shaw, T. J.; Murphy, C. J.; Wyatt, M. D. Cellular Uptake and Cytotoxicity of Gold Nanorods: Molecular Origin of Cytotoxicity and Surface Effects. *Small* **2009**, *5*, 701−708.
(47) Mahmoud, N. N.; Alhusban, A. A.; Ali, J. I.; Al-Bakri, A. G.; Hamed, R.; Khalil, E. A. Preferential Accumulation of Phospholipid-PEG and Cholesterol-PEG Decorated Gold Nanorods into Human Skin Layers and Their Photothermal-Based Antibacterial Activity. *Sci. Rep.* **2019**, *9*, 5796.
(48) Baffou, G.; Berto, P.; Bermúdez Ureña, E.; Quidant, R.; Monneret, S.; Polleux, J.; Rigneault, H. Photoinduced Heating of Nanoparticle Arrays. *ACS Nano* **2013**, *7*, 6478−6488.
(49) Baffou, G.; Quidant, R. Thermo-Plasmonics: Using Metallic Nanostructures as Nano-Sources of Heat. *Laser Photon. Rev.* **2013**, *7*, 171−187.
(50) Baffou, G.; Rigneault, H. Femtosecond-Pulsed Optical Heating of Gold Nanoparticles. *Phys. Rev. B* **2011**, *84*, No. 035415.
(51) Stujenske, J. M.; Spellman, T.; Gordon, J. A. Modeling the Spatiotemporal Dynamics of Light and Heat Propagation for in Vivo Optogenetics. *Cell Rep.* **2015**, *12*, 525.
(52) PENNES, H. H. Analysis of Tissue and Arterial Blood Temperatures in the Resting Human Forearm. *J. Appl. Physiol.* **1948**, *1*, 93−122.
(53) Witter, M. P. The Perforant Path: Projections from the Entorhinal Cortex to the Dentate Gyrus. *Prog. Brain Res.* **2007**, *163*, 43−61.
(54) Van Hoesen, G. W.; Pandya, D. N.; Butters, N. Cortical Afferents to the Entorhinal Cortex of the Rhesus Monkey. *Science* **1972**, *175*, 1471−1473.
(55) Wilson, R. C.; Steward, O. Polysynaptic Activation of the Dentate Gyrus of the Hippocampal Formation: An Olfactory Input via the Lateral Entorhinal Cortex. *Exp. Brain Res.* **1978**, *33*, 523−534.
(56) Jones, R. S. G. Entorhinal-Hippocampal Connections: A Speculative View of Their Function. *Trends Neurosci.* **1993**, *16*, 58−64.
(57) Förster, E.; Zhao, S.; Frotscher, M. Laminating the Hippocampus. *Nat. Rev. Neurosci.* **2006**, *7*, 259−268.
(58) Nilssen, E. S.; Doan, T. P.; Nigro, M. J.; Ohara, S.; Witter, M. P. Neurons and Networks in the Entorhinal Cortex: A Reappraisal of the Lateral and Medial Entorhinal Subdivisions Mediating Parallel Cortical Pathways. *Hippocampus* **2019**, *29*, 1238−1254.
(59) Lee, H.; GoodSmith, D.; Knierim, J. J. Parallel Processing Streams in the Hippocampus. *Curr. Opin. Neurobiol.* **2020**, *64*, 127−134.
(60) Chung, A.; Jou, C.; Grau-Perales, A.; Levy, E. R. J.; Dvorak, D.; Hussain, N.; Fenton, A. A. Cognitive Control Persistently Enhances Hippocampal Information Processing. *Nature* **2021**, *600*, 484−488.
(61) Hengen, K. B.; Lambo, M. E.; VanHooser, S. D.; Katz, D. B.; Turrigiano, G. G. Firing Rate Homeostasis in Visual Cortex of Freely Behaving Rodents. *Neuron* **2013**, *80*, 335−342.
(62) Goold, C. P.; Nicoll, R. A. Single-Cell Optogenetic Excitation Drives Homeostatic Synaptic Depression. *Neuron* **2010**, *68*, 512−528.
(63) Silverman, D.; Chen, C.; Chang, S.; Bui, L.; Zhang, Y.; Raghavan, R.; Jiang, A.; Le, A.; Darmohray, D.; Sima, J.; Ding, X.; Li, B.; Ma, C.; Dan, Y. Activation of Locus Coeruleus Noradrenergic Neurons Rapidly Drives Homeostatic Sleep Pressure. *Sci. Adv.* **2025**, *11*, 651.

https://doi.org/10.1021/acsnano.6c02201
ACS Nano XXXX, XXX, XXX−XXX

(64) Cook, M. J. Blood vessels of the brain. Dorsal aspect. *The Anatomy of the Laboratory Mouse*; Academic Press: London, 1965; pp 88.

https://doi.org/10.1021/acsnano.6c02201
ACS Nano XXXX, XXX, XXX−XXX